

This work was written as part of one of the author's official duties as an Employee of the United States Government and is therefore a work of the United States Government. In accordance with 17 U.S.C. 105, no copyright protection is available for such works under U.S. Law.

Public Domain Mark 1.0

<https://creativecommons.org/publicdomain/mark/1.0/>

Access to this work was provided by the University of Maryland, Baltimore County (UMBC) ScholarWorks@UMBC digital repository on the Maryland Shared Open Access (MD-SOAR) platform.

**Please provide feedback**

Please support the ScholarWorks@UMBC repository by emailing [scholarworks-group@umbc.edu](mailto:scholarworks-group@umbc.edu) and telling us what having access to this work means to you and why it's important to you. Thank you.

# A fast, accurate algorithm to account for non-Lambertian surface effects on TOA radiance

Wenhan Qin

Science Systems and Applications, Inc., Lanham, Maryland

Jay R. Herman

Atmospheric Chemistry and Dynamics Branch, NASA Goddard Space Flight Center, Greenbelt, Maryland

Ziauddin Ahmad

Science and Data Systems, Inc., Silver Spring, Maryland

**Abstract.** Surface bidirectional reflectance distribution function (BRDF) influences both the radiance just above the surface and that emerging from the top of the atmosphere (TOA). In this study we propose a new, fast, and accurate algorithm CASBIR (correction for anisotropic surface bidirectional reflection) to account for such influences on TOA radiance. This new algorithm is based on four-stream theory that separates the radiation field into direct and diffuse components in both upwelling and downwelling directions. Such a separation is important because the direct component accounts for a substantial portion of incident radiation under a clear sky, and the BRDF effect is strongest in the reflection of the incident direct radiation. The model is validated by comparison with a full-scale, vector radiative transfer model for the atmosphere-surface system [Ahmad and Fraser, 1982] for wavelengths from UV to near-IR over three typical but very different surface types. The result demonstrates that CASBIR is accurate for all solar and viewing zenith and azimuth angles considered, with overall relative difference of less than 0.7%. Application of this algorithm includes both accounting for non-Lambertian surface scattering on the emergent radiation above TOA and developing a more effective approach for surface BRDF retrieval from satellite-measured radiance. Comparison with the result from the Lambertian model indicates that surface BRDF influence on TOA radiance is both angle and wavelength dependent. It increases as solar zenith angle decreases or wavelength increases and becomes strongest in the view directions where the surface reflection is most anisotropic (such as in the hot spot or Sun glint regions).

## 1. Introduction

The radiance observed by satellites at the top of the atmosphere is the backscattered portion of incident solar radiation from the Earth's ground-atmosphere system. This radiance can be separated into two components: one from purely atmosphere backscattering (path reflection) and the other from the radiance reflected by the underlying surface and transmitted through the atmosphere toward a satellite or other instrument within the atmosphere. Traditional atmospheric radiative transfer (RT) models usually assume isotropic scattering from the lower boundary (Lambertian surface) when calculating the contribution of the underlying surface [e.g., Dave, 1964].

However, natural surfaces are usually non-Lambertian; that is, they scatter light anisotropically. They all exhibit some degree of bidirectional reflection properties. The most common is specular reflection that occurs in the scatterer's local normal plane when the incident angle is equal to the reflection angle (e.g., sun glint for water surfaces [see Breon, 1993]) and hot spot phenomenon, where the strongest backscattering occurs when the viewer is exactly behind the source light for porous

media such as vegetated surfaces [Qin and Goel, 1995]. The change in surface reflectance with both incident and viewing directions is often referred to as the surface BRDF (bidirectional reflectance distribution function) property. This property has been considered and investigated for many years by simulation of radiation propagation in porous media [Hapke, 1981] and surface reflectance modeling for vegetation cover [see Goel, 1988; Qin and Liang, 2000].

Surface BRDF affects not only radiance right above the surface but also the emergent radiance from the top of the atmosphere (TOA). Early studies for both a Rayleigh atmosphere [Coulson *et al.*, 1966] and a turbid atmosphere [Keopke and Kriebel, 1978] found significant differences between visible-wavelength radiance at TOA over natural surfaces and their Lambert-model equivalent, even though their albedos were equal. In a similar study on surface BRDF effects, Fitch [1981] combined an atmosphere-surface model with laboratory measurements of surface bidirectional reflectance for three types of natural soil surfaces. He considered polarization and multiple scattering up to 5 orders of scattering between the two media (the atmosphere and the underlying surface) in the vector radiative transfer model. Ahmad and Fraser [1982] developed a full-scale, vector RT model for the atmosphere-ocean system, in which the anisotropy of scattering from a rough ocean is incorporated. Lee and Kaufman [1986] modified

Copyright 2001 by the American Geophysical Union.

Paper number 2001JD900215.  
0148-0227/01/2001JD900215\$09.00

that model for vegetated surfaces to study non-Lambertian surface effects on upward radiance above a surface or at TOA. They found that use of the Lambertian assumption could result in a considerable error in an upward radiance calculation or in surface reflectance derivations from satellite observations.

To explicitly consider interactions between the atmosphere and an underlying non-Lambertian surface, *Tanre et al.* [1983] divided the radiation emerging at TOA into five parts: incident direct/diffuse radiation, directly/diffusely radiation transmitted through the atmosphere after surface reflection, plus a term for multiple scattering between the surface and the atmosphere. In their final formulation the multiple-scattering contribution is ignored. The 6S model [*Vermote et al.*, 1997] added a term to the above formulation trying to approximate multiple-scattering contributions. However, it was not introduced in a physically consistent manner (the authors called the arbitrary addition an approximate term in the paper) since there were no physically based derivations to justify the presence of this extra term. Further, the direct-to-diffuse (or diffuse to directional) conversion of radiation caused by surface reflection was improperly simulated.

When polarization can be neglected, the DISORT radiative transfer model is frequently a reasonably fast method to obtain accurate radiative transfer solutions, especially for larger optical depths. In a recent version of the DISORT code, *Stamnes et al.* [1988] assumed the surface BRDF to be a function only of the phase angle, so Legendre polynomials can be used to represent non-Lambertian surface reflection. Since it only represents a single angle, this assumption is not valid in general. Even for a single angle, the ability of Legendre functions to represent the surface BRDF is quite limited.

To remove formulation uncertainties in the application of such algorithms as applied to general situations, it is desirable to base the derivation of a radiative transfer approximation method on a consistent consideration of the physics. The new four-stream approximation algorithm, presented in section 2, will improve accuracy when accounting for surface BRDF, as well as providing fast computational implementation. Comparisons with a full radiative transfer treatment of the BRDF effect (using an enhanced version of the Gauss-Seidel approach based on work by *Ahmad and Fraser* [1982]) validate the accuracy of the algorithm and show the need for computational speed in a highly accurate approximation.

In section 2 we will describe the development of this new algorithm: Correction for anisotropic surface bidirectional reflection (CASBIR), including determination of the various coefficients. Then, we will compare the results with that from a precise, vector-based atmospheric radiative transfer model [*Ahmad and Fraser*, 1982] for a pure Rayleigh atmosphere. The application issues will be discussed in section 4, followed by the conclusion section.

## 2. Algorithm Development

For a Lambertian surface with surface reflectance  $r_s$ , the reflectance above the atmosphere can be expressed as follows:

$$R_a(i, v) = r_0 + \frac{T_{\downarrow}(i) \cdot r_s \cdot T^{\uparrow}(v)}{1 - S_b \cdot r_s}, \quad (1)$$

where  $i, v$  are illumination (solar) and viewing directions;  $r_0$  is the path scattering-reflectance of the atmosphere.  $T_{\downarrow}$  is the total transmittance from the top of the atmosphere to the

ground along the path of the incoming solar beam, and  $T^{\uparrow}$  is the total transmittance from the ground to the top of the atmosphere in the view direction of the satellite.  $S_b$  is the fraction of the upward diffuse flux backscattered from the atmosphere to the Earth's surface. For a non-Lambertian surface, the surface reflectance  $r_s$  changes with both illumination and viewing directions. This, combined with the anisotropic incident radiance upon the surface, means (1) could result in considerable errors in TOA radiance calculations.

Radiation incident on a surface is partially direct (plane parallel) and partially diffuse. The direct component results from transmission of the direct solar beam through the atmosphere, while the diffuse component results from atmosphere scattering of the incident solar beam and downward scattering of upwelling radiation after reflection from the surface. The BRDF effect is strongest in the reflection of the direct component, which can be more than 80% of total incident solar radiation in visible and near-infrared regions under a clear sky. To capture this BRDF effect, the direct (or collimated) component has to be treated separately from the diffuse component when modeling its interaction with the surface. Also, to completely take account of surface BRDF effects on measurements above TOA, one has to consider the conversion between direct or directional radiation and diffuse radiation from surface reflection, as well as multiple scattering between the atmosphere and the surface. These goals can be achieved by applying well-known four-stream theory [*Hapke*, 1981; *Li et al.*, 1996; *Qin and Liang*, 2000] to simulate radiation interaction in the boundary between two media.

In this study we will express radiation flux in terms of diffuse (upwelling and downwelling directions) and direct or directional (collimated in a specified direction) components. This division will ensure that a correct surface reflection coefficient is applied for a given set of incoming and outgoing radiation from surface reflection (see section 2.2.1 for details). When dealing with multiple scattering between two media, the conversion and multiple interactions among all types of radiation (downwelling and upwelling direct and diffuse) are fully taken into account with proper reflection coefficients applied, including all orders of multiple scattering. This will overcome most of the weaknesses in previous atmosphere-surface models incorporating surface BRDF characteristics in the lower boundary. Note that we only apply four-stream theory to approximate radiation interactions in the boundary between the two media, not inside the medium (atmosphere or surface). Within each medium, one can use either vector (i.e., considering polarization) or scalar RT models to produce the input atmosphere and surface parameters needed for the algorithm. This practice will ensure that the new algorithm have both high accuracy and computation speed, as proved in the validation (section 3).

### 2.1. Non-Lambertian Model

Consider an atmosphere bounded below by a non-Lambertian reflecting surface with bidirectional reflectance  $r(i, v)$ . We divide the radiation field in the atmosphere into two components (fluxes): diffuse ( $E$ ) and direct (or directional) ( $F$ ). Upward and downward arrows stand for upwelling and downwelling components with superscript (or subscript) for quantities at the upper (or lower) boundary of the atmosphere (see Figure 1). We also define  $\sigma$  as the path reflectance,  $t$  as the path transmittance, and  $r$  as the boundary reflectance. Each coefficient has two subscript symbols, “ $d$ ” (direct or directional) or “ $h$ ” (diffuse or hemispheric (i.e., the average over

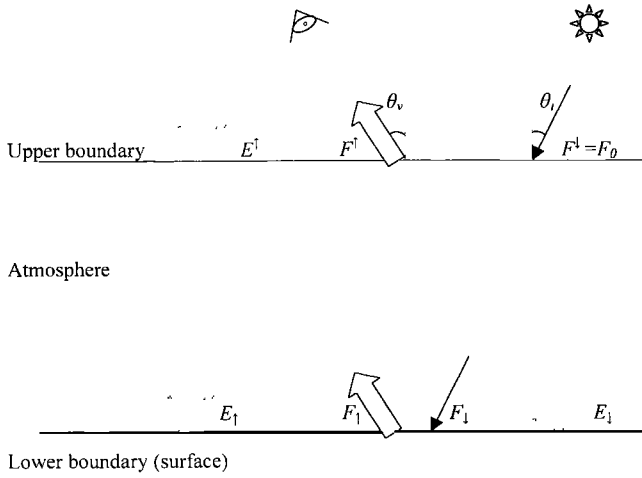


**Figure 1.** A schematic graph to illustrate radiation interaction in the upper and lower atmospheric boundaries using the four-stream scheme (see text for details).

the hemisphere)), to indicate photon status before and after interaction. Therefore there are four combinations of these two symbols: “*dd*,” “*dh*,” “*hd*,” and “*hh*,” with the first symbol indicating the initial status of photons (incoming) and the second one for the resulting photon status after interaction (outgoing). For example, subscript *dh* indicates the incoming photons from a specific direction being diffusely scattered into the whole hemisphere, either by backward atmospheric path scattering (reflection) (as in  $\sigma_{dh}$ ) or by forward path scattering (transmission) (as in  $t_{dh}$ ) or boundary reflection (as in  $r_{dh}$ ).

As shown in Figure 1, at the top of the atmosphere, the only incident radiation flux,  $F^\downarrow(i)$ , is the direct solar beam with zenith angle  $\theta_i$  and azimuth angle  $\varphi_i$ . The radiation scattered into the field of view (FOV) of the sensor in the view direction  $(\theta_v, \varphi_v)$ ,  $F^\uparrow(v)$ , is the sum of three components:

$$F^\uparrow(v) = \sigma_{dd}(i, v) \cdot F^\downarrow(i) + t_{dd}(v) \cdot F^\uparrow(v) + t_{hd}(v) \cdot E_\uparrow, \quad (2)$$

where  $F^\uparrow(v)$  is the directional radiation flux leaving the surface in direction  $v$ , and  $E_\uparrow$  is the upwelling diffuse flux from the surface. Value  $\sigma_{dd}$  is the purely atmospheric scattering coefficient for the combination of  $i$  and  $v$  (also called path reflectance, equal to  $r_0$  in (1)),  $t_{dd}$  is the direct part of  $T^\uparrow$ , i.e., atmospheric transmittance for collimated radiation in the satellite viewing direction, and  $t_{hd}$  is the diffuse part of  $T^\uparrow$ , i.e., the efficiency of atmospheric scattering of upward diffuse radiation coming from the surface toward the satellite in the viewing direction  $(\theta_v, \varphi_v)$  at TOA. We will discuss these and other coefficients in detail in section 2.2.

To calculate  $F^\uparrow(v)$ , we need to evaluate  $F^\uparrow$  and  $E_\uparrow$  first. On the basis of the above definitions, the equations to compute  $F^\uparrow$  and  $E_\uparrow$  can be written as

$$\begin{aligned} F^\uparrow(v) &= r_{dd}(i, v) \cdot F^\downarrow(i) + r_{hd}(v) \cdot E_\downarrow, \\ E_\uparrow &= r_{dh}(i) \cdot F^\downarrow(i) + r_{hh} \cdot E_\downarrow. \end{aligned} \quad (3a)$$

Equation (3a) considers the conversion between directional and diffuse radiation caused by surface reflection. The solution of the above equation set can be obtained by first evaluating first-order scattering components of  $E_\downarrow$  and  $E_\uparrow$ , then second-order components, third-order components, and so on [Li et al., 1996]. After considering all orders of multiple scattering

between the two media, the final analytical expressions for  $F^\uparrow$  and  $E_\uparrow$  can be obtained as follows:

$$\begin{aligned} F^\uparrow(v) &= r_{dd}(i, v) \cdot F^\downarrow(i) + r_{hd}(v) \cdot [t_{dh}(i) \cdot F^\downarrow(i) + \sigma_{hh} \cdot E_\uparrow], \\ E_\uparrow &= \frac{r_{dh}(i) \cdot F^\downarrow(i) + r_{hh} \cdot [t_{dh}(i) \cdot F^\downarrow(i)]}{1 - r_{hh} \cdot \sigma_{hh}}, \quad (3b) \\ F^\downarrow(i) &= t_{dd}(i) \cdot F^\downarrow(i). \end{aligned}$$

Replacing  $F^\uparrow$  and  $E_\uparrow$  in (2) with the above expressions, and after some mathematical manipulations, we finally deduce the reflectance at TOA,  $R_a$ , defined as the ratio of  $F^\uparrow(v)/F^\downarrow(i)$ , in matrix form as

$$\begin{aligned} R_a(i, v) &= \sigma_{dd}(i, v) \\ &+ \frac{\mathbf{T}(i) \cdot \mathbf{R}(i, v) \cdot \mathbf{T}(v) - t_{dd}(i) \cdot t_{dd}(v) \cdot |\mathbf{R}(i, v)| \cdot \sigma_{hh}}{1 - r_{hh} \cdot \sigma_{hh}}, \end{aligned} \quad (4a)$$

where matrices  $\mathbf{T}(i)$ ,  $\mathbf{T}(v)$ , and  $\mathbf{R}$  are defined as

$$\begin{aligned} \mathbf{T}(i) &= [t_{dd}(i) \quad t_{dh}(i)], \quad \mathbf{T}(v) = \begin{bmatrix} t_{dd}(v) \\ t_{hd}(v) \end{bmatrix}, \\ \mathbf{R}(i, v) &= \begin{bmatrix} r_{dd}(i, v) & r_{dh}(i) \\ r_{hd}(v) & r_{hh} \end{bmatrix}. \end{aligned} \quad (4b)$$

While (4a) is similar to (1) in form, with the following equivalents,

$$\begin{aligned} T^\downarrow(i) &= t_{dd}(i) + t_{dh}(i), \quad T^\uparrow(v) = t_{dd}(v) + t_{hd}(v), \\ r_0 &= \sigma_{dd}, \quad S_b = \sigma_{hh}, \quad r_s = r_{hh}, \end{aligned} \quad (4c)$$

it is different from the Lambertian model (equation (1)), since scalar variables such as  $T^\uparrow$ ,  $T^\downarrow$ , and  $r_s$  in (1) are replaced by the corresponding matrices in the non-Lambertian model (equation (4a)). Also, there is an extra term in (4a), which is a function of the determinant  $|\mathbf{R}|$ , calculated as

$$|\mathbf{R}| = |\mathbf{R}(i, v)| = r_{dd} \cdot r_{hh} - r_{dh} \cdot r_{hd}. \quad (4d)$$

Since  $|\mathbf{R}|$  can be positive or negative, depending on solar and viewing directions and the degree to which the surface is non-Lambertian, the contribution to  $R_a$  from a non-Lambertian surface could be larger or smaller than that from its Lambert equivalent. Equation (4a) converges to (1) as the surface properties approach Lambertian reflectance, because the four components in  $\mathbf{R}$  become equal to  $r_{hh}$ , and  $|\mathbf{R}| = 0$ .

## 2.2. Estimation of Various Coefficients

There are two types of coefficients involved in CASBIR (equation (4a)): atmosphere related ( $\mathbf{T}(i)$ ,  $\mathbf{T}(v)$ , each has two components, and  $\sigma$ , which has four components, even though only two ( $\sigma_{dd}$ ,  $\sigma_{hh}$ ) are used here) and surface related ( $\mathbf{R}$ , which has four components). Fortunately, as shown below, coefficients in one group are independent of those in the other group and can be determined separately. For example, atmospheric-property-related coefficients could be calculated by using any atmospheric RT model based on a Lambertian surface assumption. Similarly, components of  $\mathbf{R}$  can be determined from surface bidirectional reflectance distributions, regardless of atmospheric conditions, because surface BRDF is an intrinsic property of the surface, independent of atmospheric con-

ditions. In the following, we will describe determination of coefficients in both groups.

**2.2.1. Boundary reflection coefficients.** BRDF is a basic quantity used to characterize surface reflection. It is defined as the differential of the reflected radiance with respect to the incident irradiance for any illumination and observation directions [Nicodemus et al., 1977]. This quantity has the dimension ( $\text{sr}^{-1}$ ) and may have extremely high values (even going to infinity for an ideal specular reflector). For the Earth's surface, surface BRDF is controlled by surface structures (size, shape, and orientation of scatterers and gaps among them) and optical properties of surface constituents (material reflectivity and transmittance), and varies with illumination and observation directions.

BRDF can only be approximated when making measurements, since a sensor has a finite field of view. Therefore in practical applications, another quantity, BRF (bidirectional reflectance factor), has been commonly used as a surrogate for BRDF. BRF is defined as the ratio between radiance reflected from a real surface and that from a perfect Lambertian reflector, assuming all other conditions are the same. The use of BRF will be adopted in this study to calculate components of  $\mathbf{R}$  in (4a).

All components of  $\mathbf{R}$  are functions of surface BRF and can be calculated straightforwardly once the surface BRF is determined. In the following, we will discuss the definition and theoretical determination of components of  $\mathbf{R}$ . We leave the discussion on practical methods to determine surface BRF to section 4.

The  $r_{dd}$  – bidirectional reflectance  $r_{dd}$  can be defined in terms of the BRF,  $r(i, v)$ . That is,

$$r_{dd}(i, v) = r(i, v), \quad (5a)$$

where

$$r(i, v) = \pi I_{\uparrow}(i, v) / \mu_i F_{\downarrow}(i) \quad (5b)$$

is the surface BRF under direct solar beam (note that the above expression is valid regardless of the nature of the incident radiation (direct or diffuse or both). In CASBIR we only need BRF under direct solar radiation).  $F_{\downarrow}(i)$  is the direct solar flux incident upon the surface (see (3b)) in direction  $i$  with  $\mu_i = \cos(\theta_i)$ , and  $I_{\uparrow}(i, v)$  is the reflected radiance of  $F_{\downarrow}(i)$  from the surface in direction  $v$ . As indicated in section 4,  $r(i, v)$  can be determined by modeling or measurements for a given surface type.

The  $r_{dh}$  – directional-hemispheric reflectance  $r_{dh}$  specifies the fraction of direct radiation incident upon a surface that is diffusely reflected toward the upper hemisphere ( $2\pi^+$ ). Mathematically, it can be expressed as

$$r_{dh} = \frac{\int_{2\pi^+} I_{\uparrow}(i, \xi) \mu_{\xi} d\Omega_{\xi}}{\mu_i F_{\downarrow}(i)}, \quad (6a)$$

where  $\xi$  is the scattering direction. Replacing  $I_{\uparrow}(i, \xi)$  with  $r(i, \xi)$  in (5b) yields

$$r_{dh} = r_h(i), \quad r_h(i) = \frac{1}{\pi} \int_0^{2\pi} d\varphi_{\xi} \int_0^1 r(i, \xi) \mu_{\xi} d\mu_{\xi}. \quad (6b)$$

Value  $r_h(i)$  is the hemispheric reflectance for a specific incident (solar) direction for all viewing directions.

The  $r_{hd}$  – hemispheric-directional reflectance  $r_{hd}$  is defined as the fraction of downwelling diffuse radiation reflected toward the specific direction  $v$  by the surface; that is,

$$r_{hd}(v) = \frac{\int_{2\pi^-} L_{\uparrow}(\xi, v) \mu_{\xi} d\Omega_{\xi}}{E_{\downarrow}}, \quad (7a)$$

where integration over  $2\pi^-$  represents the lower hemisphere,  $\xi$  is the incident direction of diffuse light upon the surface, and  $L_{\uparrow}$  is the upward reflected radiance of  $E_{\downarrow}$ , which is equal to  $r(i, v) E_{\downarrow} / \pi$ . Therefore we finally have

$$r_{hd}(v) = r_h(v), \quad r_h(v) = \frac{1}{\pi} \int_0^{2\pi} d\varphi_{\xi} \int_0^1 r(\xi, v) \mu_{\xi} d\mu_{\xi}. \quad (7b)$$

Value  $r_h(v)$  is the hemispheric reflectance for a specific viewing direction for all incident directions. If the surface reflection follows the reciprocity law, i.e.,  $r(i, v) = r(v, i)$ , then  $r_h(i) = r_h(v)$  and  $r_{dh} = r_{hd}$  when  $i = v$ .

The  $r_{hh}$  – hemispheric-hemispheric reflectance  $r_{hh}$  is also called bihemispheric reflectance. By definition, it is the double integral of the scattered diffuse radiation ( $L_{\uparrow}$ ) over viewing (upper) and illumination (lower) hemispheres divided by the downwelling diffuse radiation. That is,

$$r_{hh} = \frac{\frac{1}{\pi} \int_{2\pi^+} \left\{ \int_{2\pi^-} L_{\uparrow}(\xi, \xi) \mu_{\xi} d\Omega_{\xi} \right\} \mu_{\xi} d\Omega_{\xi}}{E_{\downarrow}}, \quad (8a)$$

where  $\xi, \xi$  is the source-light and scattering direction, respectively. Similar to the calculation of  $r_{hd}$ , the above double integral can be simplified and evaluated as

$$r_{hh} = \text{albedo} = \frac{1}{\pi} \int_0^{2\pi} d\varphi_{\xi} \int_0^1 r_h(\xi) \mu_{\xi} d\mu_{\xi}, \quad (8b)$$

where  $r_h(\xi)$  is the same as  $r_h(v)$ , expressed in (7b). Therefore  $r_{hh}$  is the spherical albedo that considers all viewing and illumination directions. It is sometimes also called surface spectral albedo ( $\alpha$ ) because it only changes with surface type and wavelength.

**2.2.2. Atmospheric scattering and transmission coefficients.** Atmospheric path scattering ( $\sigma$ ) and transmission ( $T$ ) coefficients are functions of the atmospheric optical depth ( $\tau_a$ ), single-scattering albedo ( $\omega$ ), and phase function ( $P$ ) of the scatterers and absorbers in the atmosphere. Only the direct component of  $T$  (see (4b)) has an analytical expression,

$$t_{dd}(\mu) \equiv t_{dd}(\mu, \tau_a) = \exp(-\tau_a / \mu), \quad (9)$$

where  $\mu = \cos(\theta)$ ,  $\theta$  is the zenith angle of the light. Since the scattering coefficient  $\sigma_{dd}$  (path reflectance) and  $\sigma_{hh}$  (backward scattering of the upward diffuse flux from the surface) are the same as  $r_0$  and  $S_b$  in (1), their determination will not be discussed here. In the following we will only discuss the determination of the diffuse components of atmospheric transmission function  $T$ .

The  $t_{dh}$  – directional-hemispheric path transmittance  $r_{dh}$  defines the fraction of downward diffuse flux generated by atmospheric scattering as the direct solar beam passes through the atmosphere. It is also called the atmospheric diffuse trans-

mission function. Mathematically, it can be expressed as follows:

$$t_{dh}(i) = \frac{\int_{2\pi} L_{\downarrow}(i, \xi) \mu_{\xi} d\Omega_{\xi}}{\mu_i F^{\uparrow}(i)}, \quad (10)$$

where  $L_{\downarrow}$  is the downwelling diffuse radiance reaching the surface due to atmospheric scattering of the incident direct solar radiation in direction  $i$  into direction  $\xi$ . Generally, there is no analytical expressions for  $L_{\downarrow}$  because of the multiple scattering in the atmosphere. However, numerical results for  $L_{\downarrow}$  are available for a given atmosphere type from conventional atmospheric RT models. Therefore  $t_{dh}$  is usually provided in the form of a table for given solar zenith angles and atmospheric conditions (e.g., a given set of  $\tau_a$ ,  $\omega$ , and  $P$ ). Using a full RT calculation to generate an electronic look-up table for a particular parameter in the CASBIR model is an efficient and accurate method when analytical functions cannot be obtained.

The  $t_{hd}$  — hemispheric-directional path transmittance  $t_{hd}$  is defined as the fraction of upward diffuse flux scattered by atmospheric constituents (molecules and aerosols) toward the satellite in direction  $v$ . Similar to  $t_{dh}$ ,  $t_{hd}$  can be estimated from

$$t_{hd}(v) = \frac{\int_{2\pi} L^{\uparrow}(\xi, v) \mu_{\xi} d\Omega_{\xi}}{E_{\uparrow}}, \quad (11)$$

where  $L^{\uparrow}$  is the upwelling diffuse radiance at the top of the atmosphere scattered toward the viewing direction  $v$  by atmospheric constituents. For the same reasons as  $L_{\downarrow}$ ,  $L^{\uparrow}$  can only be numerically tabulated by using most standard atmospheric RT models, from which  $t_{hd}$  can be evaluated using (11).

### 3. Validation

To validate CASBIR, we compare the modeled reflectance at TOA with calculations from a full vector atmospheric RT model [Ahmad and Fraser, 1982], here called VRT model. The reason for choosing the VRT model as the standard for comparison is because of its ability to directly incorporate arbitrary surface BRDF distributions into the model. The VRT model has been successfully compared with both DISORT and the Dave vector code for Lambertian surfaces. We also use the VRT model to calculate atmosphere-related parameters ( $\sigma$  and  $T$ ) needed in CASBIR for validation purposes. We may use other resources for those parameters in practical applications (see section 4). For the validation study, we use five wavelengths (388, 443, 551, 645, and 870 nm) in a Rayleigh atmosphere, selected from Triana or MODIS channels, covering from UV to near-IR over three diverse types of surface (desert, grassland, and forest).

To obtain surface BRDF distributions, an elaborate three-dimensional (3-D) scene BRDF model [Qin et al., 1998; Qin and Gerstl, 1998, 2000] is employed to generate 3-D structures for a given surface type, which is then used in the computation of the complete BRDF distribution. The input optical properties (reflectance and transmittance of vegetation elements and the soil background) and structural parameters are taken from

field measurements [Privette et al., 2000; Walter-Shea et al., 1992; Hall et al., 1992]. For validation we prefer to use modeled surface BRFs from the 3-D scene model rather than using field BRDF measurements. This is because of its high accuracy for any heterogeneous, 3-D structures, as well as the high angular resolution of the simulated BRDF data (which enables us to accurately evaluate  $r_h$  and  $r_{hh}$ ). Also, using the modeled values allows us to complete the comparison over the whole hemisphere without having to do any interpolations for surface BRDF.

Specifically, for each surface type at each wavelength, we produced a look-up table (LUT) for surface BRDF over 16 view zenith angles (VZAs, 6° in step) and 16 relative azimuth angles (12° in step) for each solar zenith angle (SZA), with a total of 16 LUTs generated for 16 SZAs. Using these high angular resolution LUTs, we can perform a reliable numerical integration of (6b) (or (8b)) to evaluate the hemispheric reflectance  $r_h$  (or bihemispheric reflectance  $r_{hh}$ ). The results are shown in Figure 2 (in which  $\alpha$  is the spectral albedo, identical to  $r_{hh}$ ) for the three surface types. Both  $r_h$  and  $\alpha$  are highly wavelength dependent, ranging from 0.015 to 0.55 for wavelength from UV to near IR. Over desert and forest,  $r_h$  slowly but steadily decreases with SZA except at very high SZAs or in near IR for forest, while over grassland,  $r_h$  steadily increases with SZA regardless of wavelength. The structure of rolling-hill deserts (which reflects the topography of many natural deserts) produces more shadows at higher SZA in the forward directions. This reduces scene reflectance in those directions. For forest the broader hot spot effect at lower SZA results in higher hemispheric reflectance until SZA is very high, in which case the mutual shading effect and stronger backscattering predominate. Also, at wavelengths with high material reflectance and transmittance (e.g., near-IR here), the multiple-scattering component becomes stronger as optical depth increases with SZA. This makes  $r_h$  increase steadily as SZA increases in the near-IR for vegetated scenes. For grassland, the steady increase of  $r_h$  with SZA is because it has less shadowing effects than desert and weaker hot spot effect than forest due to its more architecturally homogeneous structure.

On the basis of the LUTs for surface BRDF, the VRT model calculates reflectance at TOA for the Rayleigh atmosphere overlying each non-Lambertian ground surface. Figures 3 and 4 plot surface BRDF distributions and the corresponding TOA BRFs at two wavelengths (551 and 870 nm) for the three surface types at SZA of 30°. Note that desert exhibits the largest contrast in reflectance between forward and backward directions because of its rolling-hill structure, as discussed above. Forest has the sharpest hot spot reflection peak because of the highly heterogeneous structure (large gaps in the canopy and strong scale effects), and grassland has the least variations in reflectance compared to the above two. Both grassland and forest have flat soil backgrounds. The atmospheric effect is stronger at 551 nm than at 870 nm because Rayleigh scattering decreases as wavelength increases. Comparison between surface BRDF and TOA BRDF for three other wavelengths (not shown here) indicates that surface BRDF effects on TOA radiance increase as the wavelength gets longer, because the atmospheric optical depth and path-scattering contribution get smaller.

We also calculated TOA BRFs with CASBIR with the input atmospheric parameters ( $\sigma$  and  $T$ ) provided by VRT and the surface reflection parameters (three components of  $\mathbf{R}$  with  $r_h(v) = r_h(i)$ ) computed with surface BRDF LUTs mentioned

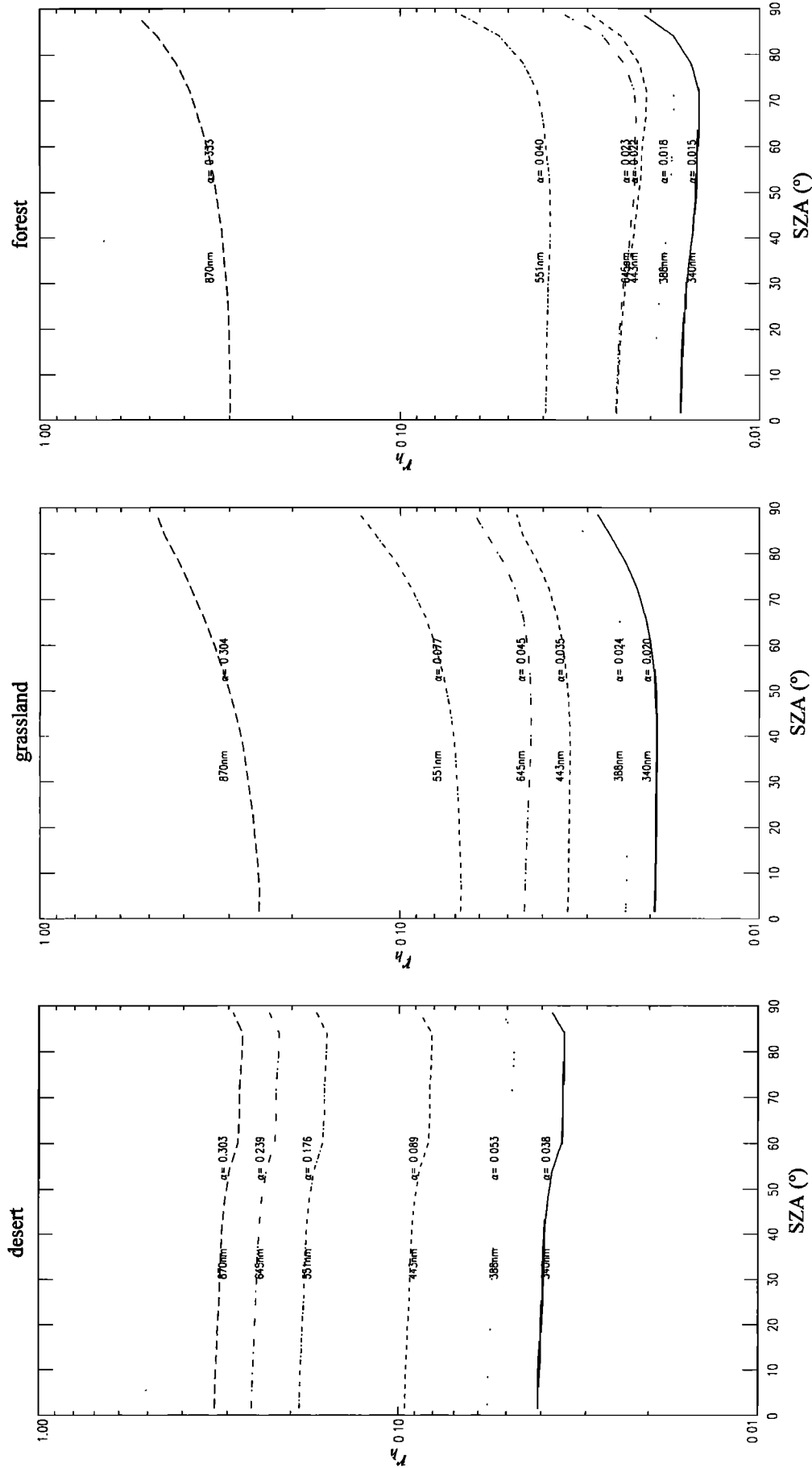
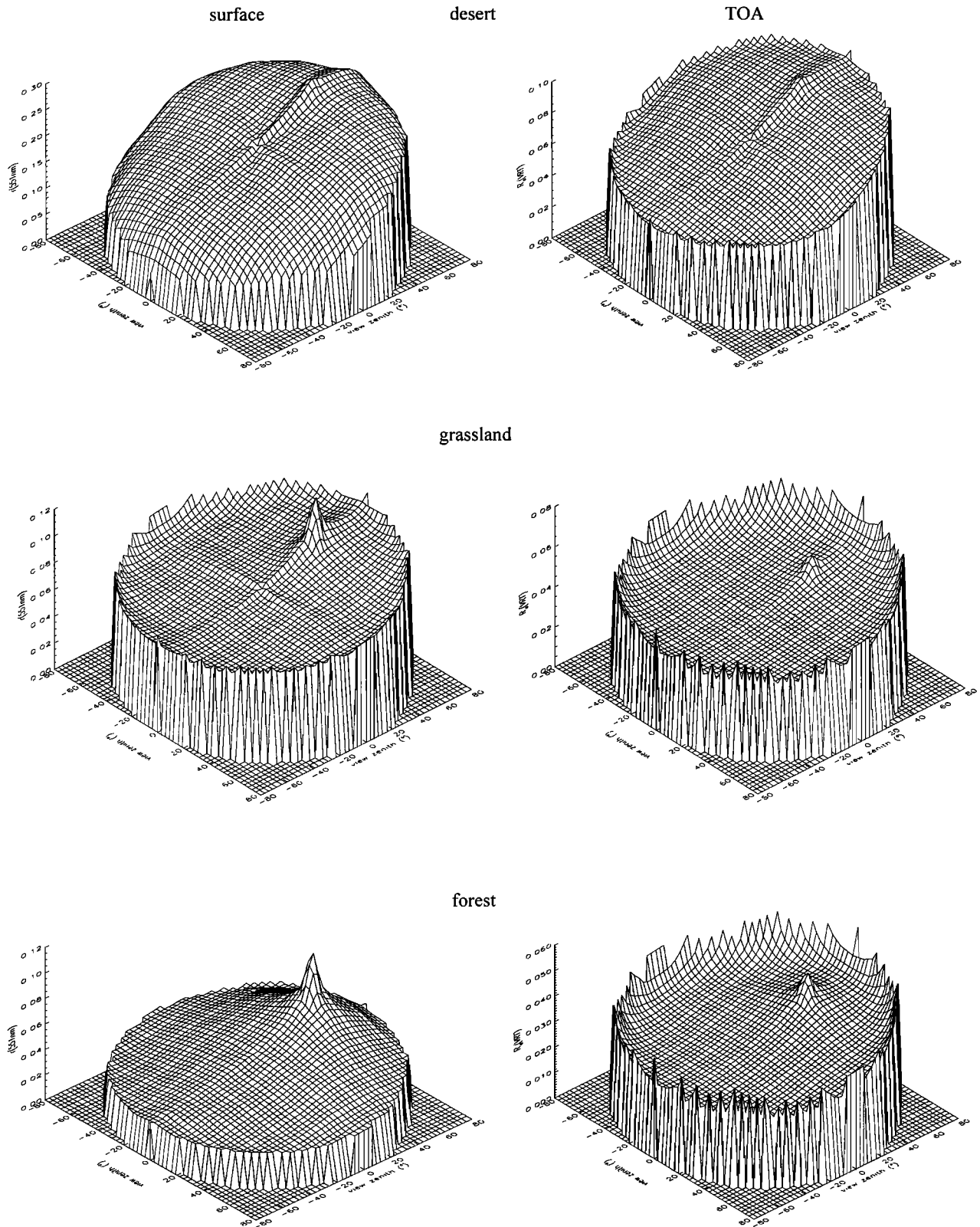
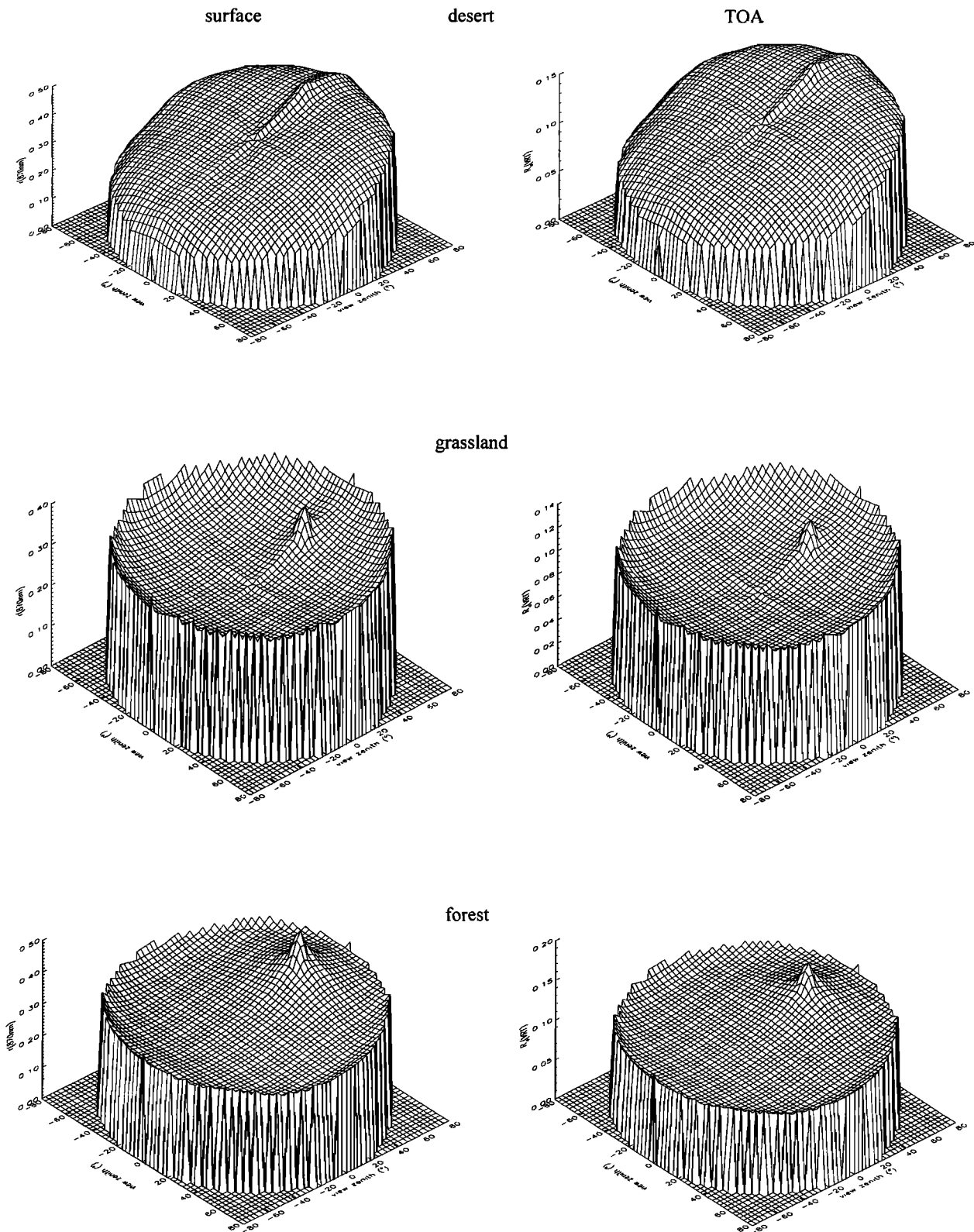


Figure 2. Albedo ( $\alpha$ ) and hemispheric surface reflectance ( $r_h$ ) varying with solar zenith angles, land types (desert, grassland, and forest), and wavelengths (340, 388, 443, 551, 645, and 870 nm).



**Figure 3.** Simulated BRFs over three different surfaces (left three plots) vs. above TOA (right three plots) at solar zenith angle of  $30^\circ$  in 551 nm. The polar coordinate system represents view zenith angle with  $0^\circ$  (nadir) at the center of the plot and  $90^\circ$  at the edge. The view azimuth angle increases clockwise with forward scattering direction at  $0^\circ$  and the hot spot direction at  $180^\circ$ .





**Figure 4.** Same as in Figure 3 but for the near-IR (870 nm).

before. The results are compared with those from VRT, as detailed in Figures 5–7 for three wavelengths (388, 551, and 870 nm) under three SZAs (6°, 30°, and 60°) in the solar principal plane (view azimuth in 0°–180° transect), and are

summarized in Table 1 for all solar and viewing directions considered (a total of 2912 angles for each surface type after excluding zenith angles larger than 80°).

Numbers in Table 1 prove that the CASBIR algorithm is

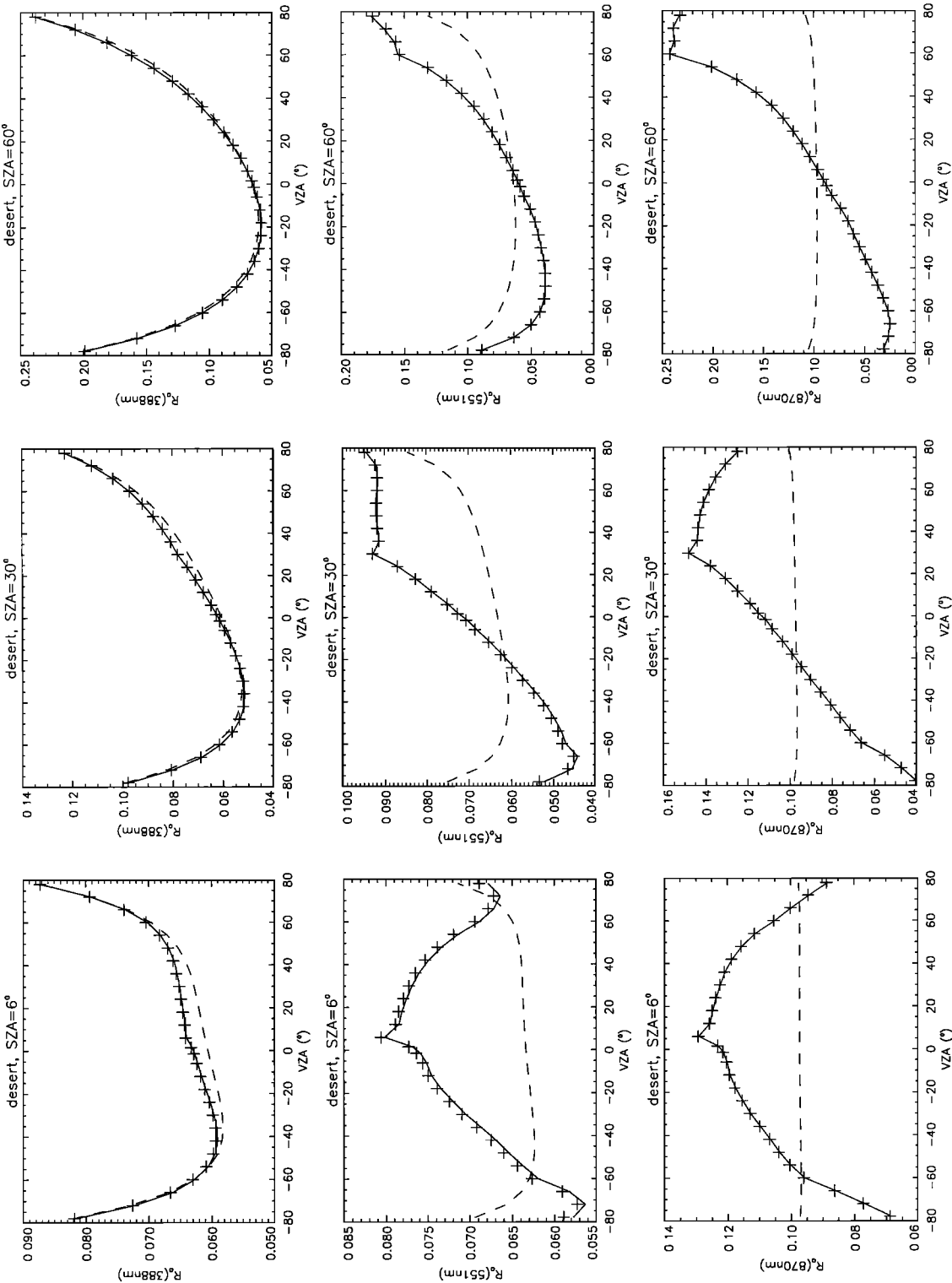


**Figure 5.** Comparison among TOA reflectances over the desert scene from the VRT model (solid line), CASBIR (plus sign) and the Lambertian equivalent (dash line) in the solar principal plane, with positive (negative) VZAs for backward (forward) directions, in 388, 551 and 870 nm (top to bottom) at solar zenith angle of 6, 30 and 60° (left to right).

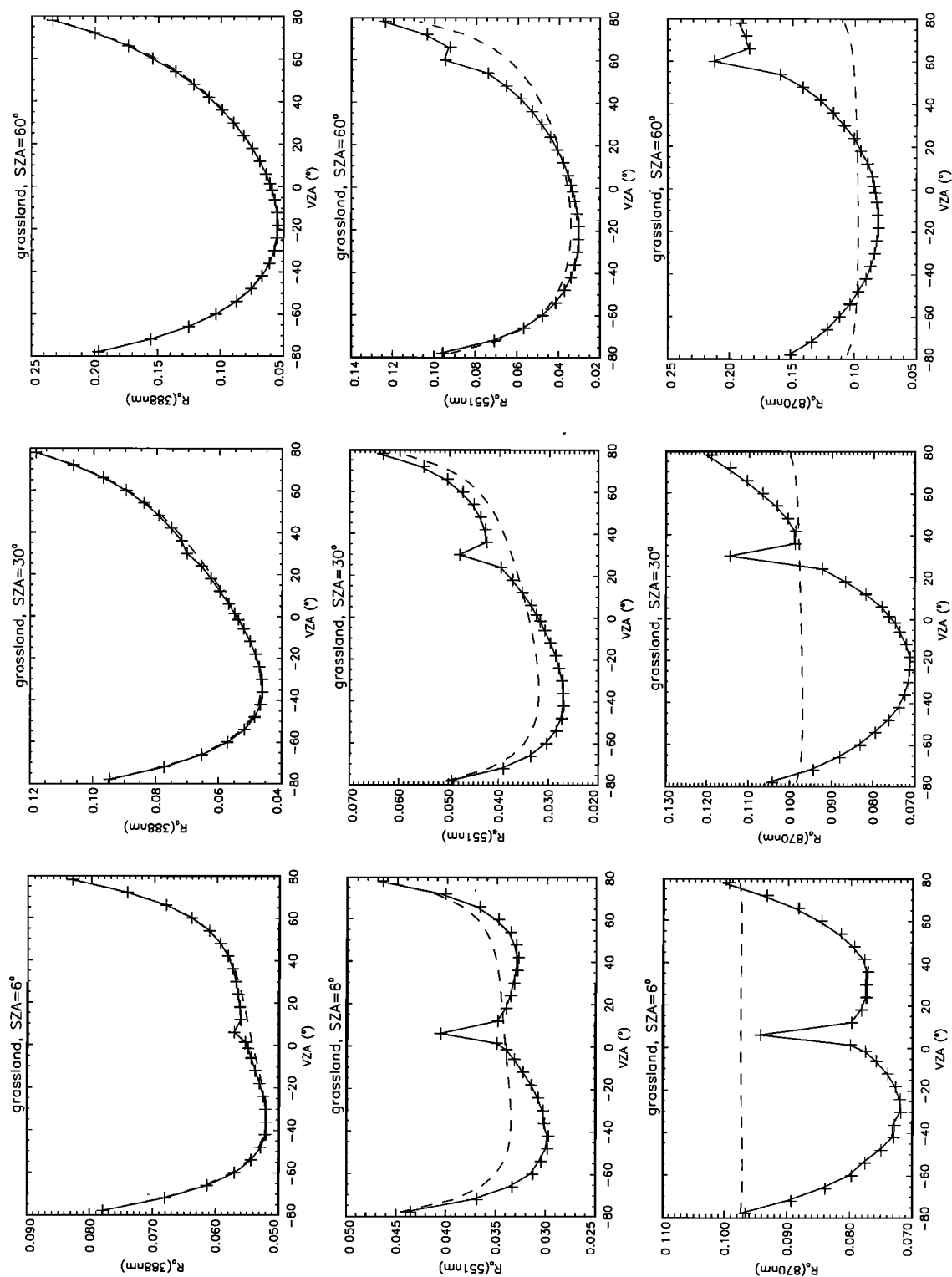


**Figure 6.** Same as in Figure 5 but over grassland.

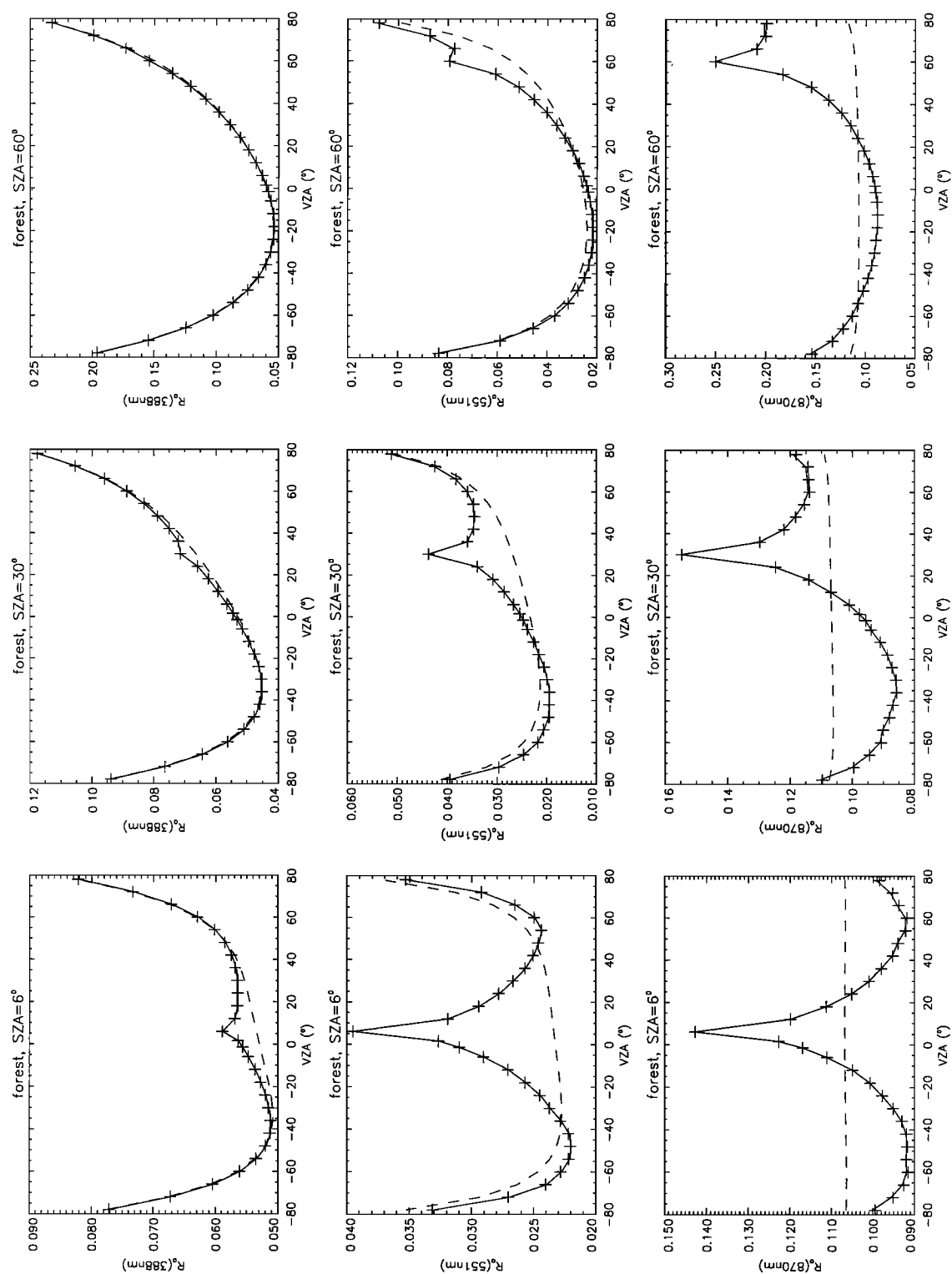


**Figure 7.** Same as in Figure 5 but over forest scene.

**Table 1.** Percentage Differences of CASBIR and Lambertian Model for All Solar and Viewing Directions Considered (Excluding Zenith Angles Larger Than 80°) Over Three Different Surface Types Under a Clear Sky (Rayleigh Atmosphere)

Wavelength, nm		388	443	551	645	870	
Desert	CASBIR	mean	0.24	0.52	0.68	0.53	0.21
		maximum	0.74	1.49	2.37	2.35	1.33
	Lambertian	mean	1.79	5.86	16.79	23.68	31.69
		maximum	5.58	18.47	78.43	151.47	300.37
	Grassland	CASBIR	mean	0.06	0.12	0.65	0.13
maximum			0.27	0.62	2.05	0.71	1.17
Lambertian		mean	0.56	1.84	7.45	8.42	19.15
		maximum	4.52	11.10	32.75	37.90	66.21
Forest		CASBIR	mean	0.11	0.24	0.24	0.23
	maximum		0.39	0.75	0.91	0.72	1.47
	Lambertian	mean	1.04	3.08	8.37	11.86	13.22
		maximum	9.43	24.18	41.07	54.53	69.31

very effective and quite accurate in accounting for surface BRDF influences at all angles. The average percentage difference is mostly below 0.5%, with the highest mean difference no more than 0.7% for all surface types and wavelengths. The average difference under Lambertian assumption, however, is much higher, with the highest up to 32% for desert in the near IR. Generally, CASBIR performs very well in matching angular distributions of the VRT model-simulated TOA BRFs in the principal plane (Figures 5–7). The percentage difference varies with VZA and wavelength. The maximum percentage differences, shown in Table 1, occur at very high VZA in the visible region. This is because we assume isotropically atmospheric backward scattering for radiance entered into the base of the atmosphere from surface reflection. This assumption may be violated at large VZAs. Also, in the visible (e.g., 551 nm) region, both surface reflectance and atmospheric scattering are relatively large, compared to cases at shorter wavelengths (where surface reflectance is pretty small, as in the UV region) or at longer wavelengths (where atmospheric scattering is very weak, as in the near IR). This explains why the maximum percentage difference appears around 551 nm in Table 1.

As a contrast, the equivalent Lambertian model (i.e.,  $r_s = r_{hh}$  in (1)) produces substantially different TOA BRDF distributions (dashed lines in Figures 5–7), especially in the hot spot region or at the visible and near-IR wavelength. The discrepancy varies with SZA and wavelength. It increases as SZA decreases (because the hot spot effect gets broader and the contribution from atmospheric path scattering gets smaller) or as the wavelength increases (because the surface reflectance becomes larger and the atmospheric scattering becomes weaker).

The above comparison demonstrates that the surface BRDF effect is wavelength dependent because of changes in surface material reflectivity with wavelength and wavelength dependence of atmosphere scattering. The percentage difference also increases with increasing view zenith angles. Finally, for a given surface type at a fixed wavelength, the surface BRDF effect varies with the type of surface formations and topography, since highly heterogeneous surfaces usually have strong anisotropic scattering and, accordingly, strong surface BRDF effects.

#### 4. Application

CASBIR has the following advantages compared to previous atmospheric RT models that consider a non-Lambertian surface boundary: (1) the number of input atmospheric parameters required is no more than for the Lambertian model (equation (1)) and see (4c)); (2) the computation time is comparable to the Lambertian model; and (3) since the average percentage difference is less than 0.7% for a Rayleigh atmosphere, it is nearly as accurate as the more computationally expensive, full-scale vector RT models that include a non-Lambertian surface boundary. This non-Lambertian model should have a wide application in areas such as accounting for surface BRDF effects on TOA radiance, as well as surface BRDF retrieval from satellite measurements. However, as in the Lambertian model, we have to determine atmospheric optical properties ( $\sigma$  and  $T$ ) in practical applications. In addition, since CASBIR considers non-Lambertian surface reflection, it requires four components of the surface reflection matrix ( $R$ ). In section 2.2 we have discussed the theoretical determination of those quantities. Now we will discuss the practical aspects on their estimation.

Because of multiple scattering, even for a pure Rayleigh atmosphere, there is no analytical expression for the atmospheric path-scattering coefficient matrix  $\sigma$  (although only two of its components,  $\sigma_{dd}$  and  $\sigma_{hh}$ , are used here) and the diffuse components of transmission matrix  $T$ . Numerical tabulation solutions are often sought to estimate those parameters. Fortunately, most atmospheric RT models can provide these coefficients in a form of either numerical solutions or look-up tables for a variety of Sun-view geometries and aerosol loadings [e.g., Dave and Gazdag, 1970]. The LUT approach is computationally more efficient, especially for practical use in an algorithm for satellite fields of view in a global data set [e.g., Dave and Furukawa, 1966]. For a Rayleigh atmosphere the differences in LUTs from different atmospheric RT models are quite small. For example, among different vector RT models, the difference is less than 0.3%, while between vector and scalar RT models, the difference ranges from 4 to 10%, depending on Sun-view geometries. However, at longer wavelengths (e.g., near IR) where the atmospheric optical depth is very small, one may be able to obtain an analytical approxima-

tion for these coefficients [Vermote and Tanre, 1992]. In this case, the analytical expression for a single-scattering process can be used as the first approximation because the contribution from multiple scattering is very small.

To estimate the four components of  $\mathbf{R}$ , we need reliable information on spatial distribution of surface bidirectional reflectance. Currently, this information is mostly obtained from the following three sources: (1) field measurements, (2) BRDF model simulations, and (3) surface BRF retrievals from satellite observations. Although field measurements can directly provide the ground truth for surface BRF, it is very labor intensive and only available for very limited areas and a few types of land cover. The need for surface BRF on a global scale cannot be met with this method. With validation, BRDF models have the capacity to generate BRF distributions globally. However, they have their own limitations: inflexible model applicability and difficulties in determining the needed model input parameters. Most parameterized BRDF models only work over specific surface types (except for 3-D models that are similar to the one used in this study), and their input parameters are not obtainable globally. The third method is to retrieve surface BRF from satellite data, as in the MODIS surface BRDF/albedo products [Strahler and Muller, 1999]. However, this kind of method still relies on a surface BRDF model to extend the sparse angular coverage of points from satellite-data-retrieved surface reflectance into high angular resolution BRF distributions.

As discussed above, most parameterized BRDF models have quite limited applicability, especially empirical or semiempirical models, such as the kernel-driven model used in the MODIS surface BRDF/albedo algorithm. This certainly affects the accuracy of BRF retrieval for different types of land cover. In addition, to retrieve surface BRF from satellite observations requires the subtraction of the atmospheric effect. The dilemma here is that the algorithm for an atmospheric-effect correction cannot produce a correct result for non-Lambertian surfaces without first knowing the surface BRF distribution.

Using CASBIR to retrieve surface BRDF from satellite measurements requires neither atmospheric correction of the satellite data nor any specific surface BRDF model to represent surface BRF distribution. Solving (4a) with multiangular satellite measurements (e.g., MISR, POLDER) can directly yield surface BRF for known atmospheric parameters, which can be retrieved in advance by using satellite measurements for wavelengths where the surface BRDF effect is minimum (such as in the UV region).

In practice, there are two issues involved in the direct retrieval method. First, mathematically, there may be no unique solution because (4a) involves both single and double integration of surface BRF. Second, for most satellites, the angular samples may not be sufficient to ensure a reliable retrieval of surface BRF. These constraints restrict the usefulness of the direct retrieval approach in some situations.

Since it is much easier and more accurate to identify surface type than to retrieve surface BRF from satellite observations, an alternative method, and probably a better way to estimate surface BRF, is to combine LUTs from a 3-D surface model generated BRF with satellite observations. That is, first to use an elaborate 3-D scene model to generate surface BRF LUTs for different conditions over every class of land cover and Sun-view geometry. Once the surface type is identified from satellite land cover classification, the surface BRDF pattern can be obtained by searching the pregenerated surface BRF

LUT database to find the closest match to the satellite measurements.

The physics behind this method is the great similarity of angular patterns of reflectance between above the surface and above the atmosphere in the near IR (see Figure 4), which indicates that the pattern of surface BRDF is well retained in satellite observations at these wavelengths (e.g., 870 nm). After the BRDF pattern in the near IR is identified, the BRDF pattern at other wavelengths can be easily obtained through the LUTs. While it is better to have more satellite-measured values of the BRF to do the LUT search, this method avoids the problem of insufficient angular samples of satellite observations. Obviously, a dedicated, highly accurate 3-D BRDF model, such as the Radiosity-Graphics Model (RGM [Qin and Gerstl, 2000]), is required to provide surface BRDF patterns based on reliable global or regional land cover maps. We will detail this approach in other papers in the context of using Triana observations combined with measurements from other satellites (such as SeaWiFS, MODIS, MISR, etc.) to estimate surface radiance and energy budget.

## 5. Conclusions

In this study we have described a new, fast but quite accurate algorithm to account for the effect of non-Lambertian surface scattering on radiation emerging from the top of the atmosphere (TOA). Rather than treating photons in every direction equally and precisely in its interaction with the surface, as in the VRT model, we group radiation entering or leaving the boundary between two media into direct and diffuse categories and treat both groups separately. The physical basis for this lies in the fact that the BRDF effect is the strongest in the reflection of the direct incident radiation, which comprises a substantial proportion in the incident radiation under a clear sky. The separation allows us to apply four-stream theory to handle the complicated problem of radiation interaction between two media (the atmosphere and underlying surface here), and to develop a simple, analytical algorithm to account for surface BRDF effects on satellite-measured radiance. Aside from obtaining the surface reflectance components (e.g., BRF, hemispheric reflectance, and albedo), this non-Lambertian model (equation (4a)) requires the same number of atmospheric parameters as the Lambertian model (equation (1)) and runs as fast as the Lambertian model, but with modeling accuracy almost as good as the full scale, vector atmospheric RT model.

The comparison with an accurate, full-scale vector atmospheric radiation transfer (VRT) model, which is capable of directly incorporating arbitrary surface BRDF as its lower boundary condition, demonstrates that the new fast algorithm is very accurate and effective. The relative difference is less than 0.7%, on average, in the spectral range from UV to near-IR for all three different surface types (desert, grassland, and forest).

The surface BRDF effect on TOA radiance is both angle and wavelength dependent. In the direction where the surface reflection is most anisotropic (such as in the hot spot or Sun glint regions), the surface BRDF influence is often strongest. It also varies with solar zenith angle (SZA), becoming stronger as SZA decreases because the hot spot effect gets broader. The surface BRDF effect increases with decreasing atmospheric optical thickness or increasing surface reflectance. For a clear-sky Rayleigh atmosphere, the surface influence increases with wavelength. For example, in the UV region the contribution of

atmospheric molecular scattering dominates, and surface reflectance is very small (less than 3% for a vegetation surface and 7% for desert or bare soil surfaces), so the surface BRDF effect on TOA UV radiation is marginal and can be neglected. As the wavelength increases, the contribution by atmosphere scattering declines and surface reflectance effect rises. Therefore in the near IR, the contribution from surface reflection dominates and TOA BRDF has almost the same shape as the surface BRDF. This suggests a new approach to retrieving surface BRDF patterns over a wide wavelength range by combining satellite observations in the near-IR with surface BRDF LUTs generated by a universal 3-D scene model.

## References

- Ahmad, Z., and R. S. Fraser, An iterative radiative transfer code for ocean-atmosphere systems, *J. Atmos. Sci.*, **39**, 656–665, 1982.
- Breon, F. M., An analytical model for the cloud-free atmosphere/ocean system reflectance, *Remote Sens. Environ.*, **43**, 179–192, 1993.
- Coulson, K. L., E. L. Gray, and G. M. B. Bouricius, Effect of surface reflection on planetary albedo, *Icarus*, **5**, 139–148, 1966.
- Dave, J. V., Meaning of successive iteration of the auxiliary equation in the theory of radiative transfer, *Astrophys. J.*, **140**, 1292–1303, 1964.
- Dave, J. V., and P. M. Furukawa, Scattered radiation in the ozone absorption bands at selected levels of a terrestrial Rayleigh atmosphere, *Meteorol. Monogr.*, **7**, 1–10, 1966.
- Dave, J. V., and J. Gazdag, A modified Fourier transform method for multiple scattering calculations in a plane parallel Mie atmosphere, *Appl. Opt.*, **9**, 1457–1466, 1970.
- Fitch, B. W., Effects of reflection by natural surfaces on the radiation emerging from the top of the Earth's atmosphere, *J. Atmos. Sci.*, **38**, 2717–2729, 1981.
- Goel, N. S., Models of vegetation canopy reflectance and their use in estimation of biophysical parameters from reflectance data, *Remote Sens. Rev.*, **4**, 1–222, 1988.
- Hall, F. G., K. F. Huemmrich, D. E. Strebel, S. J. Goetz, J. E. Nickerson, and K. D. Woods, Biophysical, morphological, canopy optical property, and productivity data from the superior national Forest, *NASA Tech. Memo. TM-104568*, 1992.
- Hapke, B., Bidirectional reflectance spectroscopy, 1, Theory, *J. Geophys. Res.*, **86**, 3039–3054, 1981.
- Koepeke, P., and K. T. Kriebel, Influence of measured reflection properties of vegetated surfaces on atmospheric radiance and its polarization, *Appl. Opt.*, **17**, 260–264, 1978.
- Lee, T., and Y. J. Kaufman, The effect of surface non-Lambertianity on remote sensing, *IEEE Trans. Geosci. Remote Sens.*, **GE-24**, 699–708, 1986.
- Li, X., et al., Simulation of path scattering and multiple bounces of photons between two media (in Chinese), *Sci. China*, **26**, 457–466, 1996.
- Nicodemus, F. E., et al., *Geometrical Considerations and Nomenclature for Reflectance*, Monogr. 160, pp. 64, Nat. Bur. Stand. (U.S.), Washington, D. C., 1977.
- Privette, J. L., et al., The EOS prototype validation exercise (PROVE) at Jornada: Overview and lessons learned, *Remote Sens. Environ.*, **74**, 1–12, 2000.
- Qin, W., and S. A. W. Gerstl, 3-D scene modeling and remote sensing applications, in *Proceedings of Progress in Electromagnetics Research Symposium*, Nantes, France, 1998.
- Qin, W., and S. A. W. Gerstl, 3-D scene modeling of semi-desert vegetation cover and its radiation regime, *Remote Sens. Environ.*, **74**, 145–162, 2000.
- Qin, W., and N. S. Goel, An evaluation of hot spot models for vegetation canopies, *Remote Sens. Rev.*, **13**, 121–159, 1995.
- Qin, W., and S. Liang, Plane-parallel canopy radiation transfer modeling: Recent advances and future directions, *Remote Sens. Rev.*, **18**, 281–305, 2000.
- Qin, W., S. A. W. Gerstl, and D. Deering, Examination of relations between NDVI and vegetation properties using simulated MISR data, *Proc. 18th Int. Geosci. Remote Sens. Symp.*, IGARSS, Seattle Wash., 1998.
- Stamnes, K., S.-C. Tsay, W. Wiscombe, and K. Jayaweera, Numerically stable algorithm for discrete-ordinate-method radiative transfer in multiple scattering and emitting layered media, *Appl. Opt.*, **27**, 2502–2509, 1988.
- Strahler, A. H., and J.-P. Muller, MODIS BRDF/albedo product: Algorithm theoretical basis document version 5.0, *NASA MODIS Prod. ID: MOD43*, 1999.
- Tanre, D., M. Herman, and P. Y. Deschamps, Influence of the atmosphere on space measurements of directional properties, *Appl. Opt.*, **22**, 733–741, 1983.
- Vermote, E. F., and D. Tanre, Analytical expressions for radiative properties of planar Rayleigh scattering media, including polarization contributions, *J. Quant. Spectrosc. Radiat. Transfer*, **47**, 305–314, 1992.
- Vermote, E. F., D. Tanre, J. L. Deuze, M. Herman, and J.-J. Morcrette, Second simulation of the satellite signal in the solar spectrum, 6S: Overview, *IEEE Trans. Geosci. Remote Sens.*, **GE-35**, 675–686, 1997.
- Walter-Shea, E. A., B. L. Blad, C. J. Hays, and M. A. Mesarch, Biophysical properties affecting vegetative canopy reflectance and absorbed photosynthetically active radiation at the FIFE site, *J. Geophys. Res.*, **97**, 18,925–18,934, 1992.
- Z. Ahmad, Science and Data Systems, Inc., Silver Spring, MD 20906, USA.
- J. R. Herman, Atmospheric Chemistry and Dynamics Branch, NASA Goddard Space Flight Center, Greenbelt, MD 20771, USA.
- W. Qin, GSFC NASA, Code 916, Greenbelt, MD 20771, USA. (wqin@dmouse.gsfc.nasa.gov)

(Received September 29, 2000; revised March 29, 2001; accepted April 6, 2001.)